

DIRECT COMPUTATION OF NOISE GENERATED BY VISCOUS FLOWS OVER AIRFOILS USING A HIGH-ORDER IMMERSED BOUNDARY METHOD

Rudner Lauterjung Queiroz, rudner.queiroz@embraer.com.br

Instituto Tecnológico de Aeronáutica, Campo Montenegro, IEA – ITA, CTA, São José dos Campos, SP

Roberto Francisco Bobenrieth Miserda, rfbm@unb.br

Universidade de Brasília, Campus Univ. Darcy Ribeiro, FT – ENM, Asa Norte, Brasília, DF

Marcos Aurélio Ortega, ortega@ita.br

Instituto Tecnológico de Aeronáutica, Campo Montenegro, IEA – ITA, CTA, São José dos Campos, SP

Daniel Ammirante da Cunha, daniel.ammirante@gmail.com

Universidade de Brasília, Campus Univ. Darcy Ribeiro, FT – ENM, Asa Norte, Brasília, DF

Abstract. *The objective of this work is to directly compute the noise produced by laminar flows over a NACA 0012 airfoil using a fourth-order immersed boundary method. The unsteady and compressible Navier-Stokes equations are numerically solved using a finite volume discretization where the fluxes are computed using the skew-symmetric form of Ducros' explicit fourth-order numerical scheme. The time marching process is achieved using a third-order Runge-Kutta scheme proposed by Shu. The immersed boundary method is based on a discrete forcing approach where the boundary conditions are directly imposed in the control volumes that contain the immersed boundary points, resulting in a sharp representation of the solid boundary since a null velocity is imposed in the boundary volumes. At these volumes, pressure and temperature are obtained by imposing a null value for the spatial derivatives of these variables in the outward normal direction from the solid wall. The spatial derivatives at the boundary volumes are calculated with a fourth-order accuracy, and thus preserving the overall spatial accuracy of the numerical scheme. In order to avoid the numerical oscillations resulting from the discrete forcing approach applied at initial conditions, a pseudo-force and its associated pseudo-work are introduced in the right-hand side of the momentum and energy equations that gradually accelerate, using a non-inertial frame of reference, the entire flow field from the stagnation to the free-flow condition. Aeroacoustics results are presented for two-dimensional laminar flows over a NACA 0012 airfoil at a null angle of attack and compared with available results in the bibliography and other simulations made in commercial CFD software.*

Keywords: *Aeroacoustics, immersed boundary, high-order schemes, compressible flow.*

1. INTRODUCTION

The term immersed boundary method was first used in reference to a method developed by Peskin (1972) to simulate cardiac mechanics and associated blood flow. The distinguishing feature of this method was that the entire simulation was carried out on a Cartesian grid, which did not conform to the geometry of the heart, and a novel procedure was formulated by imposing the effect of the immersed boundary on the flow. Since Peskin (1972) introduced this method, numerous modifications and refinements have been proposed and a number of variants of this approach now exist. Initially, the immersed boundary methods were developed for incompressible viscous flows. Only recently, immersed boundary methods for compressible viscous flows have been developed, and examples for this type of application are the works of de Tullio et al. (2007), Cho et al. (2006), Liu and Vasilyev (2007), and Ghias et al. (2007). In all these works the resulting numerical schemes are second-order accurate in space and time.

The objective of this work is to directly compute the noise produced by laminar flows over a NACA 0012 airfoil using a fourth-order immersed boundary method, first presented by Bobenrieth et al. (2009).

The aerodynamic noise generated by an airfoil trailing edge is an interesting problem in Aeroacoustics, being studied for several years. Tam (1974) presented experimental results of the discrete tones emitted by isolated airfoils under certain operating conditions. Brooks et al. (1989) presented a semi-empirical model for airfoils broadband self-noise. McAlpine et al. (1999) e Nash et al. (1999) studied the effects of the Tollmien-Schlichting instability waves as a mechanism of tonal noise generation. Recently, Desquesnes et al. (2007) performed a numerical investigation of the tonal noise phenomenon over laminar airfoils by direct numerical simulations, Kingan and Pearse (2009) have studied the instabilities produced by the laminar boundary layer of NACA 0012 and Sandberg et al. (2008) made several direct numerical simulations of the tonal noise emitted by NACA airfoils in laminar flows.

2. MATHEMATICAL MODEL

The unsteady compressible Navier-Stokes equations can be written in a conservation-law form as:

$$\frac{\partial \rho}{\partial t} + \frac{\partial}{\partial x_i} (\rho u_i) = 0, \quad (1)$$

$$\frac{\partial}{\partial t} (\rho u_i) + \frac{\partial}{\partial x_j} (\rho u_i u_j) = -\frac{\partial p}{\partial x_i} + \frac{\partial \tau_{ij}}{\partial x_j} + f_i, \quad (2)$$

$$\frac{\partial}{\partial t} (\rho e_T) + \frac{\partial}{\partial x_i} (\rho e_T u_i) = -\frac{\partial}{\partial x_i} (p u_i) + \frac{\partial}{\partial x_i} (\tau_{ij} u_j) - \frac{\partial q_i}{\partial x_i} + f_i u_i. \quad (3)$$

where the nondimensional variables used in the above equations are defined as:

$$x = \frac{x^*}{L^*}, \quad y = \frac{y^*}{L^*}, \quad z = \frac{z^*}{L^*}, \quad t = \frac{t^*}{L^*/U_\infty^*}, \quad u = \frac{u^*}{U_\infty^*}, \quad v = \frac{v^*}{U_\infty^*}, \quad w = \frac{w^*}{U_\infty^*}, \quad (4)$$

$$p = \frac{p^*}{\rho_\infty^* (U_\infty^*)^2}, \quad \rho = \frac{\rho^*}{\rho_\infty^*}, \quad T = \frac{T^*}{T_\infty^*}, \quad e = \frac{e^*}{(U_\infty^*)^2}, \quad \mu = \frac{\mu^*}{\mu_\infty^*}, \quad f = \frac{f^*}{\rho_\infty^* (U_\infty^*)^2 / L^*}.$$

and the asterisk indicates dimensional variables.

The viscous stress tensor is given by

$$\tau_{ij} = \frac{1}{\text{Re}_\infty} (\mu S_{ij}) = \frac{1}{\text{Re}_\infty} \left\{ \mu \left[\left(\frac{\partial u_i}{\partial x_j} + \frac{\partial u_j}{\partial x_i} \right) - \frac{2}{3} \delta_{ij} \frac{\partial u_k}{\partial x_k} \right] \right\}, \quad (5)$$

where the Reynolds number is defined as

$$\text{Re}_\infty = \frac{\rho_\infty^* U_\infty^* L^*}{\mu_\infty^*}, \quad (6)$$

The total energy is given by the sum of the internal and kinetic energy as

$$e_T = e + e_k = c_v T + \frac{u_i u_i}{2} \quad (7)$$

and the heat-flux density vector is

$$q_i = -\frac{\mu}{(\gamma - 1) M_\infty^2 \text{Re}_\infty \text{Pr}} \left(\frac{\partial T}{\partial x_i} \right), \quad (8)$$

where the Mach and the Prandtl numbers are respectively defined as

$$M_\infty = \frac{U_\infty^*}{a_\infty^*} = \frac{U_\infty^*}{\sqrt{\gamma R^* T_\infty^*}}, \quad \text{Pr} = \frac{c_p^* \mu_\infty^*}{k_\infty^*}. \quad (9)$$

In this work, the Prandtl number is considered a constant with the value 0.72. For a thermally and calorically perfect gas, the equation of state can be written as

$$p = (\gamma - 1) \rho e \quad (10)$$

and

$$T = \frac{\gamma M_\infty^2 p}{\rho}. \quad (11)$$

The molecular viscosity is obtained using Sutherland's formula

$$\mu = C_1 \frac{T^{3/2}}{T + C_2}, \quad C_1 = \left[\frac{(T_\infty^*)^{1/2}}{\mu_\infty^*} \right] C_1^*, \quad C_2 = \frac{C_2^*}{T_\infty^*}, \quad (12)$$

where C1 and C2 are constants.

3. NUMERICAL METHOD

In order to numerically solve the unsteady compressible Navier-Stokes equations using a finite volume approach, Eqs. (1), (2) and (3) are written in the vector form proposed by Anderson et al. (1983),

$$\frac{\partial \mathbf{U}}{\partial t} + \frac{\partial \mathbf{E}}{\partial x} + \frac{\partial \mathbf{F}}{\partial y} + \frac{\partial \mathbf{G}}{\partial z} = \mathbf{R}, \quad (13)$$

where the vectors \mathbf{U} , \mathbf{E} , \mathbf{F} , \mathbf{G} and \mathbf{R} are given by

$$\mathbf{U} = \begin{bmatrix} \rho \\ \rho u \\ \rho v \\ \rho w \\ \rho e_T \end{bmatrix}, \quad (14)$$

$$\mathbf{E} = \begin{bmatrix} \rho u \\ \rho u^2 + p - \tau_{xx} \\ \rho uv - \tau_{xy} \\ \rho uw - \tau_{xz} \\ (\rho e_T + p)u - u\tau_{xx} - v\tau_{xy} - w\tau_{xz} + q_x \end{bmatrix}, \quad (15)$$

$$\mathbf{F} = \begin{bmatrix} \rho v \\ \rho vu - \tau_{xy} \\ \rho v^2 + p - \tau_{yy} \\ \rho vw - \tau_{yz} \\ (\rho e_T + p)v - u\tau_{xy} - v\tau_{yy} - w\tau_{yz} + q_y \end{bmatrix}, \quad (16)$$

$$\mathbf{G} = \begin{bmatrix} \rho w \\ \rho wu - \tau_{xz} \\ \rho wv - \tau_{yz} \\ \rho w^2 + p - \tau_{zz} \\ (\rho e_T + p)w - u\tau_{xz} - v\tau_{yz} - w\tau_{zz} + q_z \end{bmatrix}, \quad (17)$$

$$\mathbf{R} = \begin{bmatrix} 0 \\ f_x \\ 0 \\ 0 \\ f_x u \end{bmatrix}. \quad (18)$$

Defining tensor Π as

$$\mathbf{\Pi} = \mathbf{E} \otimes \mathbf{i} + \mathbf{F} \otimes \mathbf{j} + \mathbf{G} \otimes \mathbf{k}, \quad (19)$$

Eq. (13) is rewritten as

$$\frac{\partial \mathbf{U}}{\partial t} + \nabla \cdot \mathbf{\Pi} = \mathbf{R}, \quad (20)$$

Integrating the above equation over the control volume V , and applying the divergence theorem to the right-hand side results

$$\frac{\partial}{\partial t} \int_V \mathbf{U} dV = - \int_V (\nabla \cdot \mathbf{\Pi}) dV + \int_V \mathbf{R} dV = - \int_S (\mathbf{\Pi} \cdot \mathbf{n}) dS + \int_V \mathbf{R} dV, \quad (21)$$

defining the volumetric mean of the vector $\bar{\mathbf{U}}$ and $\bar{\mathbf{R}}$ in the control volume V as

$$\bar{\mathbf{U}} \equiv \frac{1}{V} \int_V \mathbf{U} dV \quad (22)$$

and

$$\bar{\mathbf{R}} \equiv \frac{1}{V} \int_V \mathbf{R} dV, \quad (23)$$

Eq. (21) is written as

$$\frac{\partial \bar{\mathbf{U}}}{\partial t} = -\frac{1}{V} \int_S (\boldsymbol{\Pi} \cdot \mathbf{n}) dS + \bar{\mathbf{R}}. \quad (24)$$

For the volume (i,j,k), the first-order approximation of the temporal derivative is given by

$$\left(\frac{\partial \bar{\mathbf{U}}}{\partial t} \right)_{i,j,k} = \frac{\Delta \bar{\mathbf{U}}_{i,j,k}}{\Delta t} + O(\Delta t), \quad (25)$$

and the temporal approximation of Eq. 24 for a hexahedral control volume is

$$\begin{aligned} \Delta \bar{\mathbf{U}}_{i,j,k} = & -\frac{\Delta t}{V_{i,j,k}} \left[\int_{S_{i+1/2}} (\boldsymbol{\Pi} \cdot \mathbf{n}) dS + \int_{S_{i-1/2}} (\boldsymbol{\Pi} \cdot \mathbf{n}) dS + \right. \\ & + \int_{S_{j+1/2}} (\boldsymbol{\Pi} \cdot \mathbf{n}) dS + \int_{S_{j-1/2}} (\boldsymbol{\Pi} \cdot \mathbf{n}) dS + \\ & \left. + \int_{S_{k+1/2}} (\boldsymbol{\Pi} \cdot \mathbf{n}) dS + \int_{S_{k-1/2}} (\boldsymbol{\Pi} \cdot \mathbf{n}) dS \right] + \Delta t \bar{\mathbf{R}} \end{aligned} \quad (26)$$

where $S_{i+1/2}$, $S_{i-1/2}$, $S_{j+1/2}$, $S_{j-1/2}$, $S_{k+1/2}$ e $S_{k-1/2}$ are the surfaces that define the hexahedral control volume and $S_{i+1/2}$ is the common surface between volume (i,j,k) and volume (i+1,j,k).

Considering that the value of tensor $\boldsymbol{\Pi}$ is constant over the control surfaces, it is possible to define $\mathcal{F}(\bar{\mathbf{U}})_{i,j,k}$ as a function of the flux of tensor $\boldsymbol{\Pi}$ over the control surfaces as

$$\begin{aligned} \mathcal{F}(\bar{\mathbf{U}})_{i,j,k} = & -\frac{\Delta t}{V_{i,j,k}} \left[(\boldsymbol{\Pi} \cdot \mathbf{S})_{i+1/2} + (\boldsymbol{\Pi} \cdot \mathbf{S})_{i-1/2} + \right. \\ & + (\boldsymbol{\Pi} \cdot \mathbf{S})_{j+1/2} + (\boldsymbol{\Pi} \cdot \mathbf{S})_{j-1/2} + \\ & \left. + (\boldsymbol{\Pi} \cdot \mathbf{S})_{k+1/2} + (\boldsymbol{\Pi} \cdot \mathbf{S})_{k-1/2} \right] + \Delta t \bar{\mathbf{R}} \end{aligned} \quad (27)$$

and the resulting spatial approximation of Eq. 27 is

$$\Delta \bar{\mathbf{U}}_{i,j,k} = \mathcal{F}(\bar{\mathbf{U}})_{i,j,k} + \mathcal{D}(\bar{\mathbf{U}})_{i,j,k}, \quad (28)$$

where $\mathcal{D}(\bar{\mathbf{U}})_{i,j,k}$ is an explicit artificial dissipation. In order to calculate $\mathcal{F}(\bar{\mathbf{U}})_{i,j,k}$, the flux of tensor $\boldsymbol{\Pi}$ over the control surfaces must be calculated. For the control surface $S_{i+1/2}$, this flux is given by

$$(\boldsymbol{\Pi} \cdot \mathbf{S})_{i+1/2} = \begin{bmatrix} (\boldsymbol{\Pi} \cdot \mathbf{S})_1 \\ (\boldsymbol{\Pi} \cdot \mathbf{S})_2 \\ (\boldsymbol{\Pi} \cdot \mathbf{S})_3 \\ (\boldsymbol{\Pi} \cdot \mathbf{S})_4 \\ (\boldsymbol{\Pi} \cdot \mathbf{S})_5 \end{bmatrix}_{i+1/2}. \quad (29)$$

The first component of the vector defined by the above equation is associated to the continuity equation and given by

$$(\boldsymbol{\Pi} \cdot \mathbf{S})_1 = \rho_{i+1/2} (q_s)_{i+1/2}, \quad (30)$$

where the volumetric flux is

$$(q_s)_{i+1/2} = \mathbf{u}_{i+1/2} \cdot \mathbf{S}_{i+1/2} = u_{i+1/2} (s_x)_{i+1/2} + v_{i+1/2} (s_y)_{i+1/2} + w_{i+1/2} (s_z)_{i+1/2}. \quad (31)$$

The second, third, and fourth components are associated to the three components of the momentum equation and are respectively given by

$$\begin{aligned} (\boldsymbol{\Pi} \cdot \mathbf{S})_2 = & (\rho u)_{i+1/2} (q_s)_{i+1/2} + p_{i+1/2} (s_x)_{i+1/2} - \\ & [(\mu)_{i+1/2} (S_{xx})_{i+1/2}] (s_x)_{i+1/2} - [(\mu)_{i+1/2} (S_{xy})_{i+1/2}] (s_y)_{i+1/2}, \\ & [(\mu)_{i+1/2} (S_{xz})_{i+1/2}] (s_z)_{i+1/2} \end{aligned} \quad (32)$$

$$(\Pi \cdot S)_3 = (\rho v)_{i+1/2} (q_s)_{i+1/2} + p_{i+1/2} (s_y) - \left[(\mu)_{i+1/2} (s_{yx})_{i+1/2} \right] (s_x)_{i+1/2} - \left[(\mu)_{i+1/2} (s_{yy})_{i+1/2} \right] (s_y)_{i+1/2} - \left[(\mu)_{i+1/2} (s_{yz})_{i+1/2} \right] (s_z)_{i+1/2} \quad (33)$$

and,

$$(\Pi \cdot S)_4 = (\rho w)_{i+1/2} (q_s)_{i+1/2} + p_{i+1/2} (s_z) - \left[(\mu)_{i+1/2} (s_{xz})_{i+1/2} \right] (s_x)_{i+1/2} - \left[(\mu)_{i+1/2} (s_{yz})_{i+1/2} \right] (s_y)_{i+1/2} - \left[(\mu)_{i+1/2} (s_{zz})_{i+1/2} \right] (s_z)_{i+1/2} \quad (34)$$

The fifth component is associated with the energy equation and given by

$$(\Pi \cdot S)_5 = (\rho e_T)_{i+1/2} (q_s)_{i+1/2} + p_{i+1/2} (s_x)_{i+1/2} - u_{i+1/2} (s_x)_{i+1/2} \left[\mu_{i+1/2} (s_{xx})_{i+1/2} \right] - v_{i+1/2} (s_y)_{i+1/2} \left[\mu_{i+1/2} (s_{yy})_{i+1/2} \right] - w_{i+1/2} (s_z)_{i+1/2} \left[\mu_{i+1/2} (s_{zz})_{i+1/2} \right] - \left[u_{i+1/2} (s_y)_{i+1/2} + v_{i+1/2} (s_x)_{i+1/2} \right] \left[\mu_{i+1/2} (s_{xy})_{i+1/2} \right] - \left[u_{i+1/2} (s_z)_{i+1/2} + w_{i+1/2} (s_x)_{i+1/2} \right] \left[\mu_{i+1/2} (s_{xz})_{i+1/2} \right] - \left[v_{i+1/2} (s_z)_{i+1/2} + w_{i+1/2} (s_y)_{i+1/2} \right] \left[\mu_{i+1/2} (s_{yz})_{i+1/2} \right] - \left[k_{i+1/2} (\partial T / \partial x)_{i+1/2} \right] (s_x)_{i+1/2} - \left[k_{i+1/2} (\partial T / \partial y)_{i+1/2} \right] (s_y)_{i+1/2} - \left[k_{i+1/2} (\partial T / \partial z)_{i+1/2} \right] (s_z)_{i+1/2} \quad (35)$$

In order to calculate the flux $(\Pi \cdot S)$ according to Eqs. 30 to 35, it is necessary to approximate the values of the variables at the control surface $S_{i+1/2}$ from the mean values of the conservative variables in the control volumes, given by the vector

$$\bar{U}_{i,j,k} = \begin{bmatrix} \bar{\rho} \\ \bar{\rho u} \\ \bar{\rho v} \\ \bar{\rho w} \\ \bar{\rho e_T} \end{bmatrix}_{i,j,k} \quad (36)$$

In order to obtain the momentum and energy primitive variables, the Favre (Anderson et al., 1983) mean is used to calculate the mass-averaged momentum and energy primitive variables.

The scheme proposed is a centered one, and therefore, an explicit artificial viscosity was previously included in Eq. 28. In order to enhance the numerical method with shock-capturing capabilities and the ability to cope with steep gradient regions, this artificial dissipation uses the basic idea proposed by Jameson et al. (1981) given by

$$\mathcal{D}(\bar{U}) = \frac{\Delta t}{V_{i,j,k}} \left[d_{i+1/2}(\bar{U}) - d_{i-1/2}(\bar{U}) \right] + \left[d_{j+1/2}(\bar{U}) - d_{j-1/2}(\bar{U}) \right] + \left[d_{k+1/2}(\bar{U}) - d_{k-1/2}(\bar{U}) \right] \quad (37)$$

where

$$d_{i+1/2}(\bar{U}) = \varepsilon_{i+1/2}^{(2)} \left[(\bar{U})_{i+1} - (\bar{U})_i \right] - \varepsilon_{i+1/2}^{(4)} \left[(\bar{U})_{i+2} - 3(\bar{U})_{i+1} + 3(\bar{U})_i - (\bar{U})_{i-1} \right] \quad (38)$$

The first and second terms of Eq. 38 are second-order and fourth-order dissipation operators, respectively. The first one acts in the shock and the second one acts over steep gradient regions, like the viscous regions. The coefficients of Eq. 38 are given by

$$\varepsilon_{i+1/2}^{(2)} = K^{(2)} \max(\psi_i \phi_i, \psi_{i+1} \phi_{i+1}), \varepsilon_{i+1/2}^{(4)} = \max \left[0, (K^{(4)} - \varepsilon_{i+1/2}^{(2)}) \right] \quad (39)$$

where

$$K^{(2)} = 1/4 \quad e \quad K^{(4)} = 1/256 \quad (40)$$

Sensors ψ_i and ϕ_i are given by

$$\Psi_i = \frac{|\tilde{p}_{i+1} - 2\tilde{p}_i + \tilde{p}_{i-1}|}{\tilde{p}_{i+1} + 2\tilde{p}_i + \tilde{p}_{i-1}}, \quad \Phi_i = \frac{(\nabla \cdot \underline{u})^2}{(\nabla \cdot \underline{u})^2 + |\nabla \times \underline{u}|^2 + \varepsilon}, \quad \varepsilon = 10^{-30}, \quad (41)$$

being \tilde{p} the calculated mean value of pressure and \underline{u} the Favre mean of velocity.

The sensor Ψ_i , proposed by Jameson et al. (1981), is pressure-based and it is intended to detect shock waves. The function of sensor Φ_i , proposed by Ducros et al. (1999), is to inhibit sensor Ψ_i in regions where the divergence is low, but the rotational of the velocity field is high, like a pure vortex wake. In regions where the divergence and the rotational are high, like the vortex-shock interaction, the inhibiting capacity of sensor Φ_i decreases.

In order to advance Eq. 28 in time, a third-order Runge-Kutta is used as proposed by Shu and reported by Yee (1997). This yield to the following three steps:

$$\begin{aligned} \bar{\mathbf{U}}^1 &= \bar{\mathbf{U}}^n - \left[\mathcal{F}(\bar{\mathbf{U}}^n) - \mathcal{D}(\bar{\mathbf{U}}^n) + \Delta t \bar{\mathbf{R}}^n \right] \\ \bar{\mathbf{U}}^2 &= \frac{3}{4} \bar{\mathbf{U}}^n + \frac{1}{4} \bar{\mathbf{U}}^1 - \frac{1}{4} \left[\mathcal{F}(\bar{\mathbf{U}}^1) - \mathcal{D}(\bar{\mathbf{U}}^1) + \Delta t \bar{\mathbf{R}}^1 \right], \\ \bar{\mathbf{U}}^{n+1} &= \frac{1}{3} \bar{\mathbf{U}}^n + \frac{2}{3} \bar{\mathbf{U}}^2 - \frac{2}{3} \left[\mathcal{F}(\bar{\mathbf{U}}^2) - \mathcal{D}(\bar{\mathbf{U}}^2) + \Delta t \bar{\mathbf{R}}^2 \right] \end{aligned} \quad (42)$$

As used in this work, the resulting numerical method is shock-capturing and fourth-order accurate in space and third-order accurate in time.

4. IMMERSSED BOUNDARY TECHNIQUE

The approach used in this work for imposing the boundary conditions at the boundary volumes, defined as the control volumes that contain one or more surface-grid points, is a discrete forcing one where the boundary conditions are directly imposed to the boundary volumes. In all the control volumes, the mean values of the conservative variables are given by

$$\bar{\mathbf{U}}_{i,j,k} = \begin{bmatrix} \bar{\rho} \\ \bar{\rho u} \\ \bar{\rho v} \\ \bar{\rho w} \\ \bar{\rho e_T} \end{bmatrix}_{i,j,k}. \quad (43)$$

In the boundary volumes, the no-slip condition directly results in the boundary values

$$\tilde{u} = \tilde{v} = \tilde{w} = 0. \quad (44)$$

Since the total energy is the sum of the internal and kinetic energy, the application of the no-slip condition results in

$$\tilde{e_T} = \underline{e}, \quad (45)$$

bearing, for the boundary volumes

$$\bar{\mathbf{U}}_{i,j,k}^b = \begin{bmatrix} \bar{\rho} \\ 0 \\ 0 \\ 0 \\ \underline{e} \end{bmatrix}_{i,j,k}, \quad (46)$$

where the superscript b indicates that the finite volume ($i; j; k$) is a boundary volume. It is important to note that the number of boundary volumes is less or equal to the number of surface points, since more than one surface point can lie within one boundary volume.

In order to obtain the boundary values for the density, $\bar{\rho}$, and the internal energy, e , the averaged equation of state,

$$\underline{p} = \left(\frac{1}{\gamma M_\infty^2} \right) \bar{\rho T} \quad (47)$$

is derived in the normal outward direction from the solid wall. With this objective, it is defined \mathbf{n} as a unit vector with an outward direction that is normal to the wall, where the Cartesian components are $\mathbf{n} = n_x \mathbf{i} + n_y \mathbf{j} + n_z \mathbf{k}$ and the

magnitude is $|\mathbf{n}| = \sqrt{n_x^2 + n_y^2 + n_z^2} = 1$. Depending on the resolution of the Cartesian and surface grids, more than one surface point can lie within a boundary volume, and in this case it is used the mean among all normal unit vectors associated to the grid points that lie within the boundary volume. The normal direction was defined by one unit vector in the boundary volume or by an averaged unit vector over the boundary volume. The derivative in this normal direction is given by

$$\frac{\partial \bar{p}}{\partial n} = \left(\frac{1}{\gamma M_\infty^2} \right) \frac{\partial}{\partial n} (\bar{\rho} \bar{T}) = \left(\frac{1}{\gamma M_\infty^2} \right) \left(\bar{\rho} \frac{\partial \bar{T}}{\partial n} + \bar{T} \frac{\partial \bar{\rho}}{\partial n} \right). \quad (48)$$

For an adiabatic wall, $\partial \bar{T} / \partial n = 0$, and considering the boundary-layer approximation, $\partial \bar{p} / \partial n = 0$, Eq. (48) yields

$$\frac{\partial \bar{\rho}}{\partial n} = 0, \quad (49)$$

and since

$$\underline{e} = \frac{1}{\gamma(\gamma-1)M_\infty^2} \bar{T}, \quad (50)$$

the adiabatic wall condition results in

$$\frac{\partial \underline{e}}{\partial n} = 0, \quad (51)$$

Defining \mathbf{n} as a unit vector with an outward direction that is normal to the solid wall with Cartesian components $\mathbf{n} = n_x \mathbf{i} + n_y \mathbf{j} + n_z \mathbf{k}$, the derivatives of the averaged density and internal energy are written as

$$\frac{\partial \bar{\rho}}{\partial n} = \frac{\partial \bar{\rho}}{\partial x} \frac{\partial x}{\partial n} + \frac{\partial \bar{\rho}}{\partial y} \frac{\partial y}{\partial n} + \frac{\partial \bar{\rho}}{\partial z} \frac{\partial z}{\partial n} = n_x \frac{\partial \bar{\rho}}{\partial x} + n_y \frac{\partial \bar{\rho}}{\partial y} + n_z \frac{\partial \bar{\rho}}{\partial z} \quad (52)$$

and

$$\frac{\partial \underline{e}}{\partial n} = \frac{\partial \underline{e}}{\partial x} \frac{\partial x}{\partial n} + \frac{\partial \underline{e}}{\partial y} \frac{\partial y}{\partial n} + \frac{\partial \underline{e}}{\partial z} \frac{\partial z}{\partial n} = n_x \frac{\partial \underline{e}}{\partial x} + n_y \frac{\partial \underline{e}}{\partial y} + n_z \frac{\partial \underline{e}}{\partial z}. \quad (53)$$

For the boundary volumes, Eqs. (49) and (51) apply and result in

$$0 = n_x \left(\frac{\partial \bar{\rho}}{\partial x} \right)_{i,j,k}^b + n_y \left(\frac{\partial \bar{\rho}}{\partial y} \right)_{i,j,k}^b + n_z \left(\frac{\partial \bar{\rho}}{\partial z} \right)_{i,j,k}^b \quad (54)$$

and

$$0 = n_x \left(\frac{\partial \underline{e}}{\partial x} \right)_{i,j,k}^b + n_y \left(\frac{\partial \underline{e}}{\partial y} \right)_{i,j,k}^b + n_z \left(\frac{\partial \underline{e}}{\partial z} \right)_{i,j,k}^b. \quad (55)$$

If $n_x > 0$, in regular region of the Cartesian grid the derivative $\partial \bar{\rho} / \partial x$ in the boundary volumes can be calculated with fourth-order spatial precision using a forward finite-difference approach as

$$\left(\frac{\partial \bar{\rho}}{\partial x} \right)_{i,j,k}^b = \frac{1}{12\Delta x} \left[-25\bar{\rho}_{i,j,k}^{-b} + 48\bar{\rho}_{i+1,j,k}^{-b} - 36\bar{\rho}_{i+2,j,k}^{-b} + 16\bar{\rho}_{i+3,j,k}^{-b} - 3\bar{\rho}_{i+4,j,k}^{-b} + O(\Delta x)^4 \right]. \quad (56)$$

Defining the difference operator

$$D_i^+ \bar{\rho} = \frac{1}{25} (48\bar{\rho}_{i+1,j,k} - 36\bar{\rho}_{i+2,j,k} + 16\bar{\rho}_{i+3,j,k} - 3\bar{\rho}_{i+4,j,k}), \quad (57)$$

Eq. (56) is written as

$$\left(\frac{\partial \bar{\rho}}{\partial x} \right)_{i,j,k}^b = \frac{25}{12\Delta x} \left[\bar{\rho}_{i,j,k}^{-b} + D_i^+ \bar{\rho} + O(\Delta x)^4 \right]. \quad (58)$$

If $\mathbf{n} = \mathbf{i}$ ($n_x = 1$, $n_y = 0$ and $n_z = 0$), Eq. (54) gives

$$0 = \left(\frac{\partial \bar{\rho}}{\partial x} \right)_{i,j,k}^b, \quad (59)$$

and introducing this result in Eq. (58) yields

$$\bar{\rho}_{i,j,k}^{-b} = D_i^+ \bar{\rho} + O(\Delta x)^4. \quad (60)$$

Following the same line of reasoning, if $\mathbf{n} = \mathbf{j}$ ($n_x = 0$, $n_y = 1$ and $n_z = 0$),

$$\bar{\rho}_{i,j,k}^{-b} = D_j^+ \bar{\rho} + O(\Delta y)^4, \quad (61)$$

and if $\mathbf{n} = \mathbf{k}$ ($n_x = 0$, $n_y = 0$ and $n_z = 1$),

$$\bar{\rho}_{i,j,k}^{-b} = D_k^+ \bar{\rho} + O(\Delta z)^4. \quad (62)$$

For the generalized case, where $\mathbf{n} = n_x \mathbf{i} + n_y \mathbf{j} + n_z \mathbf{k}$, the averaged density is calculated in the boundary volumes as the weighted value

$$\bar{\rho}_{i,j,k}^{-b} = \frac{|n_x| D_i \bar{\rho} + |n_y| D_j \bar{\rho} + |n_z| D_k \bar{\rho}}{|n_x| + |n_y| + |n_z|}. \quad (63)$$

Following an analogous procedure, since $\partial \bar{\rho} / \partial n = \partial e / \partial n = 0$, the averaged internal energy is calculated as the weighted value

$$\bar{e}_{i,j,k}^{-b} = \frac{|n_x| D_i e + |n_y| D_j e + |n_z| D_k e}{|n_x| + |n_y| + |n_z|}, \quad (64)$$

where the difference operators (D_i , D_j and D_k) can be in the forward direction (D_i^+ , D_j^+ and D_k^+), if the values of n_x , n_y and n_z are positive, or in the backward direction (D_i^- , D_j^- and D_k^-), if the values of n_x , n_y and n_z are negative. For the case of the averaged density, the operator D_i^+ is given by Eq. (57), and the other forward and backward difference operators are given by

$$D_j^+ \bar{\rho} = \frac{1}{25} (48 \bar{\rho}_{i,j+1,k} - 36 \bar{\rho}_{i,j+2,k} + 16 \bar{\rho}_{i,j+3,k} - 3 \bar{\rho}_{i,j+4,k}), \quad (65)$$

$$D_k^+ \bar{\rho} = \frac{1}{25} (48 \bar{\rho}_{i,j,k+1} - 36 \bar{\rho}_{i,j,k+2} + 16 \bar{\rho}_{i,j,k+3} - 3 \bar{\rho}_{i,j,k+4}), \quad (66)$$

$$D_i^- \bar{\rho} = \frac{1}{25} (48 \bar{\rho}_{i-1,j,k} - 36 \bar{\rho}_{i-2,j,k} + 16 \bar{\rho}_{i-3,j,k} - 3 \bar{\rho}_{i-4,j,k}), \quad (67)$$

$$D_j^- \bar{\rho} = \frac{1}{25} (48 \bar{\rho}_{i,j-1,k} - 36 \bar{\rho}_{i,j-2,k} + 16 \bar{\rho}_{i,j-3,k} - 3 \bar{\rho}_{i,j-4,k}), \quad (68)$$

$$D_k^- \bar{\rho} = \frac{1}{25} (48 \bar{\rho}_{i,j,k-1} - 36 \bar{\rho}_{i,j,k-2} + 16 \bar{\rho}_{i,j,k-3} - 3 \bar{\rho}_{i,j,k-4}). \quad (69)$$

In this manner, the conservative variables vector for the boundary volumes is given by

$$\bar{\mathbf{U}}_{i,j,k}^{-b} = \begin{bmatrix} \bar{\rho}_{i,j,k}^{-b} \\ 0 \\ 0 \\ 0 \\ \bar{e}_{i,j,k}^{-b} \end{bmatrix}, \quad (70)$$

where the first and last components are given by Eqs. (63) and (64), respectively.

5. RESULTS

The proposed immersed boundary method, applied to the numerical code called *Virtual Aeroacoustic Tunnel* (VAT), developed by the Computational Aeroacoustics Laboratory (LAAC) of the University of Brasilia (UnB), was used to simulate two cases. The first one, called C1, studies a flow over a NACA 0012 airfoil with a Reynolds number of 780 thousand and a Mach number of 0.107. The second case, called C2, studies a flow over a NACA 0012 airfoil with a Reynolds number of 20 million and a Mach number of 0.4. The case C1 was chosen for a comparison of the results presented by Brooks et al. (1989). This case was also chosen for a comparison with a commercial noise simulating tool called non-linear acoustic solver (NLAS) present at the Metacomp Technologies CAA++ software. The case C2 was chosen to study the method's capability of simulating high-Reynolds compressible flows. The results of these simulations are presented next.

5.1. Case C1: Low Speed NACA 0012

The Aeroacoustics of the NACA 0012 profile with a null angle of attack for a Reynolds number of 780000 and a Mach number of 0.107 was studied. In this case, in order to achieve the proposed relation of Reynolds number and

Mach number, a chord value of 0.3048m is used. This value is exactly the same chord value of the one used by Brooks et al. (1989) in their work.

The surface grid generated for this case has 12001 points defining the geometry, allowing a Cartesian grid of 3,750,000 volumes, being 2,800,000 at the regular region of the grid. The simulation, showed a field with several weak acoustic waves propagating from the airfoil's trailing edge. Some galloping vortexes, which are the vortexes propagating over the airfoil surface were presented. Figure 1 shows a plot of $|\nabla T|^{1/20}$. This plot is interesting because the root approximates the values of the proprieties, allowing the visualization of both fluid-dynamic and acoustic phenomena in the same plot, while temperature has shown to be the most sensitive variable.

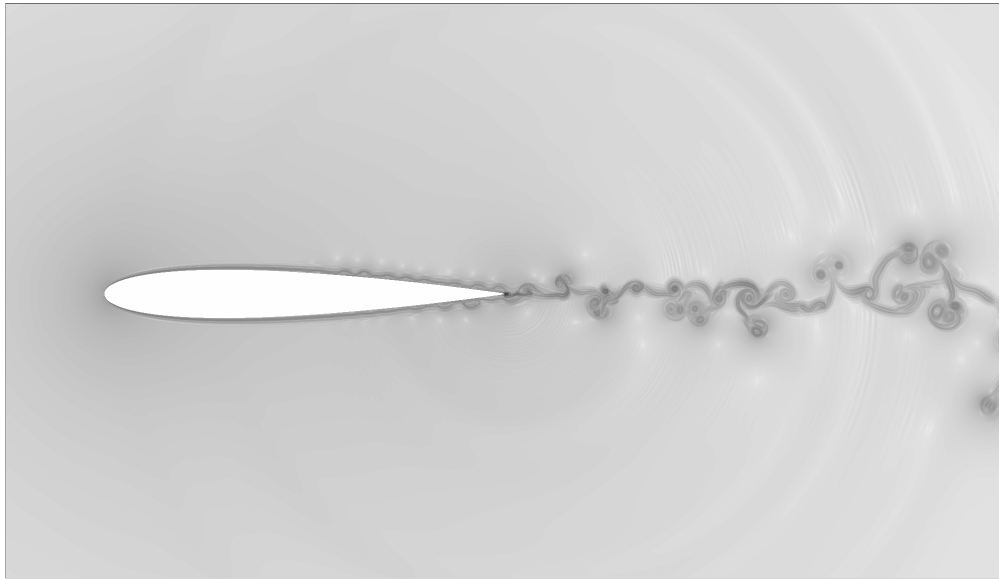


Figure 1: Acoustic field of $|\nabla T|^{1/20}$ for de case **C1**.

5.2. Case C1: Low Speed NACA 0012. NLAS Simulation

For comparing the results of the immersed boundary simulations, another methodology was used. The nonlinear low disturbances equations, proposed by Batten et al. (2004), were used inside Metacomp Technologies CFD++ package. This method, called non-linear acoustic solver (NLAS), presents an anisotropic turbulence synthesizing and requires information of the mean field by a previous RANS simulation. The two-dimensional grid was developed using the ICEM CFD software, having 440000 volumes overall, being 900 volumes over the airfoil's surface. Figure 2 below present the grid refinement at the trailing edge.

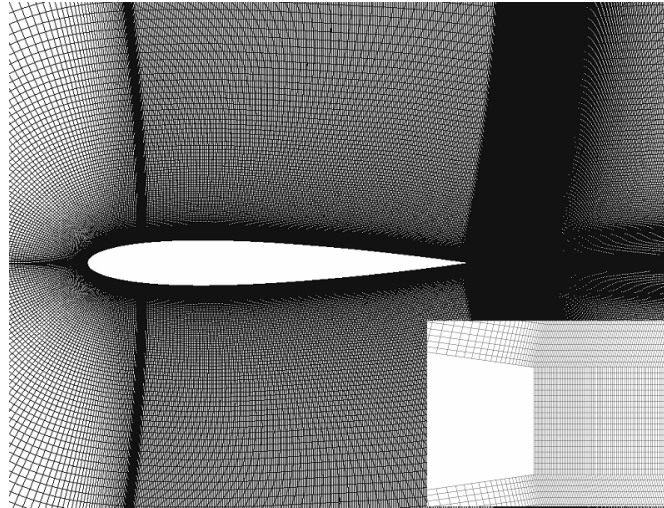


Figure 2: Computational grid used in CFD++.

The Reynolds number used was 780000 and the Mach number was 0.107, the same condition presented by Brooks et al. (1989). The field has presented an interesting vortex shedding at the trailing edge. This vortex shedding induced the appearance of some galloping vortexes. The vortex shedding also caused some weak sound emission. Those structures can be visualized at Figure 3, where the field of $|\nabla\rho|^{1/20}$ is presented. The waves are the clearer regions propagating outwards the field. It is also possible to see the boundary layer instabilities, which are in the clearer points near the body.

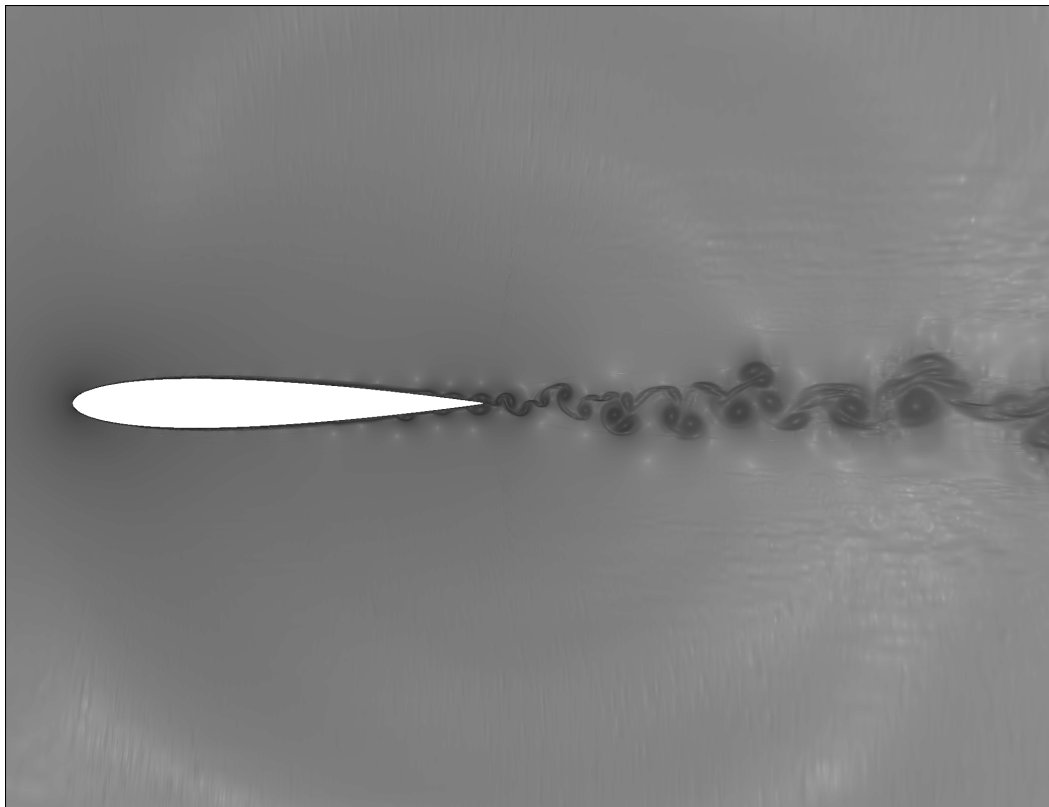


Figure 3: Acoustic field visualization of the NLAS simulation.

A pressure probe was put in the field at 0.33m from the trailing edge of the airfoil, perpendicularly, in order to evaluate the sound emission of the geometry. The signal of acoustic pressure is presented in Figure 4. Figure 5 presents the spectrum in narrowband. It is possible to see a broadband behavior of the signal, in agreement with the results presented by Brooks et al. (1989).

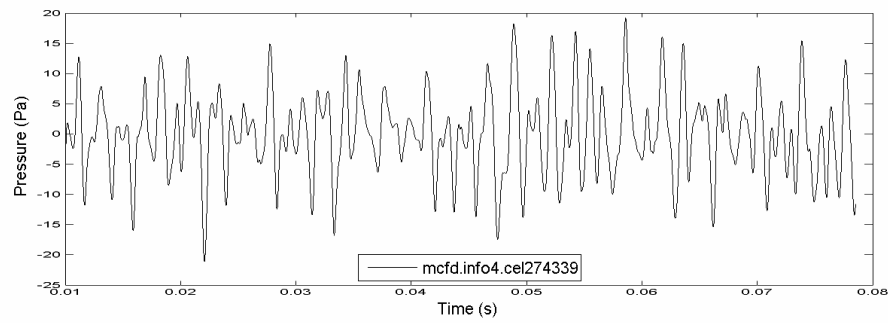


Figure 4: Pressure fluctuation signal of the NLAS probe.

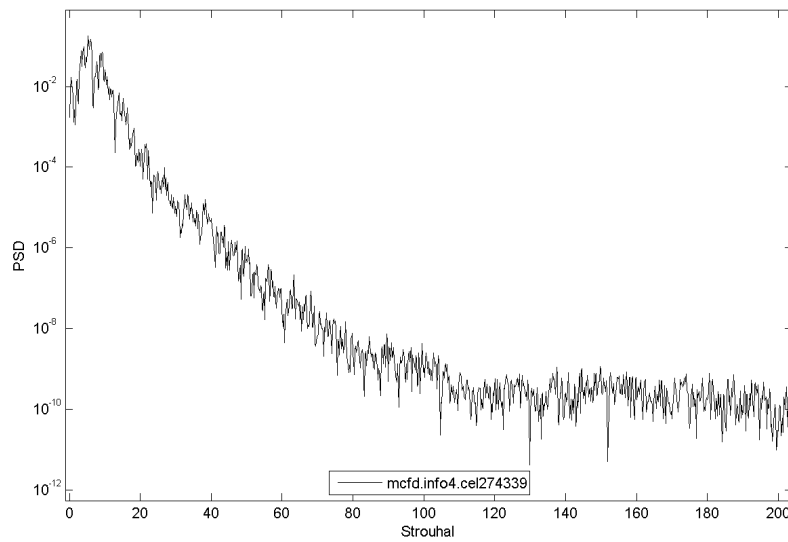


Figure 5: Narrowband spectrum of PSD for the NLAS probe.

In addition, a comparison of the $|\nabla\rho|^{1/20}$ field obtained by the NLAS and the proposed immersed boundary method (VAT) is presented at Figure 6. There, it is possible to see a good agreement between the vortex structures of both simulations, considering their diameters and emission frequency. It is also possible to see in both simulations the galloping vortices over the profile, being generated at the same region.

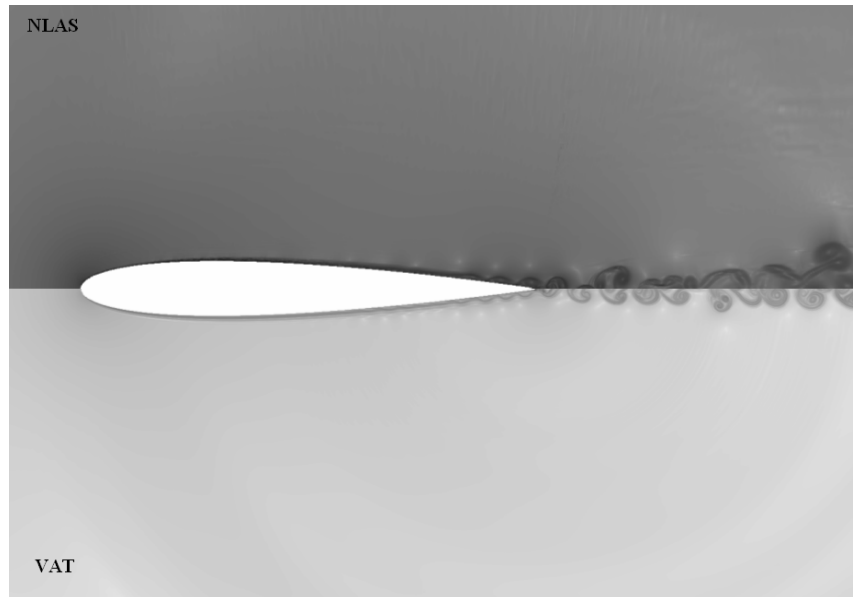


Figure 6: Fields comparison among NLAS and VAT.

5.3. Case C2: Higher Speed NACA 0012

The Aeroacoustics of the NACA 0012 profile with a null angle of attack for a Reynolds number of 20,000,000 and a Mach number of 0.4 was studied in this case. In this case, a more aeronautical condition was simulated. Against the 0.3048m chord used in case C1, a value of 2.26m was used.

The surface grid generated for this case has 4581 points defining the geometry, allowing a Cartesian grid of 3,240,000 volumes, being 2,200,000 at the regular region of the grid. The simulation, similarly to the C1 results, showed an interesting pressure field, with several acoustic waves propagating from the airfoil's trailing edge. The galloping vortexes were also presented. Figure 7 shows a plot of $|\nabla T|^{1/20}$. In sequence, Figure 8 and Figure 9 present the acoustic pressure signal and its respective power spectrum density curves for some probes at: the silence region, which is the region right in front of the leading edge; the noise region, which is represented by a probe right below the trailing edge, perpendicularly to the undisturbed flow; and the pseudo-noise region, which is the region of vortex passing, right behind the trailing edge. All probes are 3.0 chords distant from the airfoil's trailing edge.

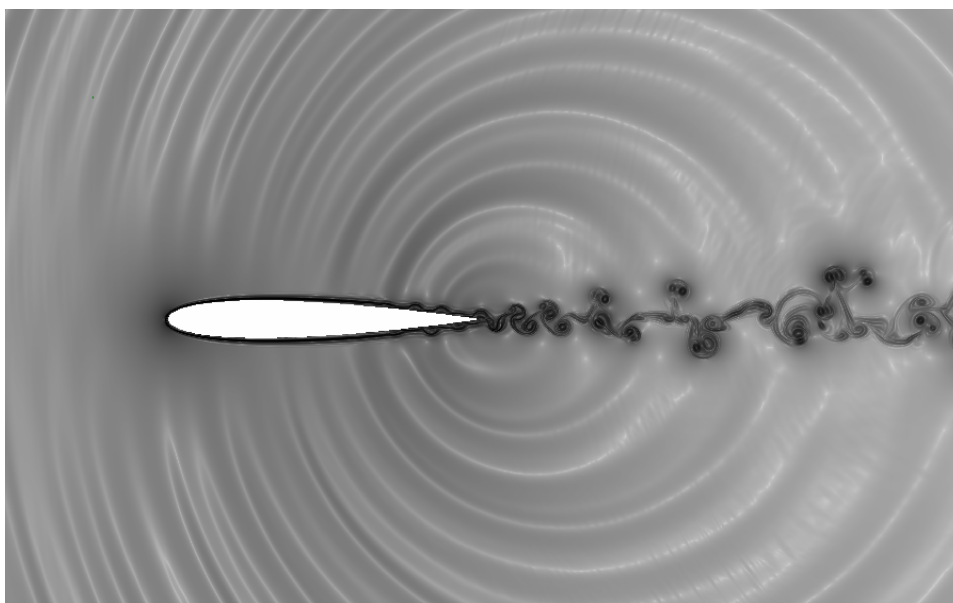


Figure 7: Acoustic field of $|\nabla T|^{1/20}$ for de case C2.

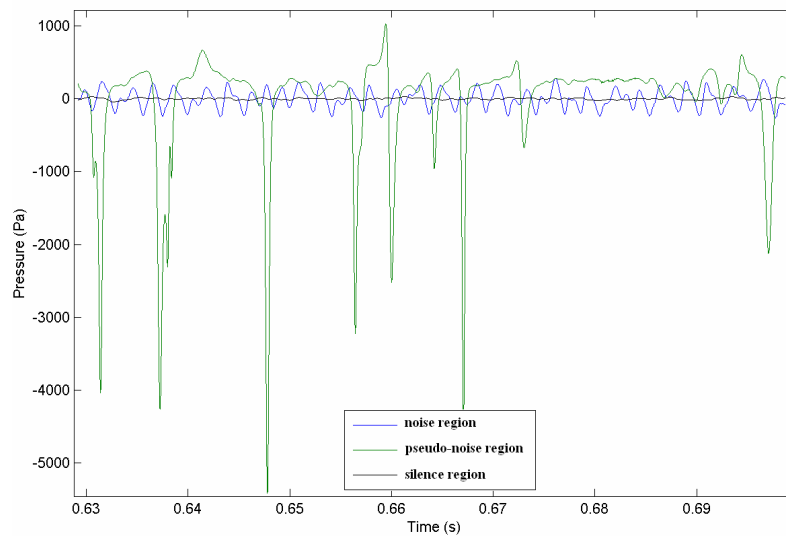


Figure 8: Pressure fluctuation signals of the C2 probes.

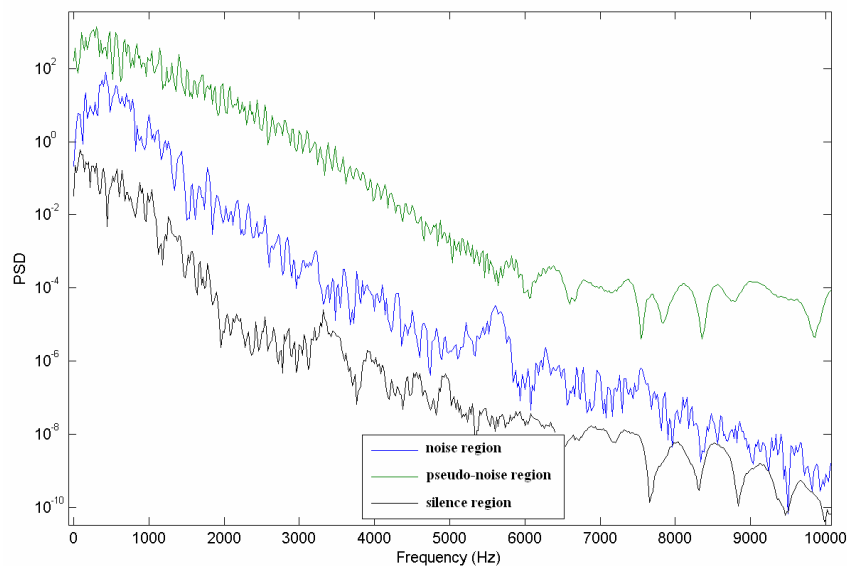


Figure 9: Narrowband spectra of PSD for the C2 probes.

6. CONCLUDING REMARKS

With the simulations of NACA 0012 airfoil, it was possible to notice the broadband noise emitted by its trailing edge. The visualizations have presented as the main sources of this noise the vortex emission at the trailing edge and the vortex convalescence among the wake. The similarity of the results presented by both C1 simulations using VAT and Metacomp's NLAS have demonstrated well the usage of those methods in aeroacoustic problems. The spectra presented by the case C2 at the silence region, noise region and the pseudo-noise region have demonstrated very different behaviors on it, as much as the different sound levels of those regions. A next step of this study is the simulation of NACA 0012 airfoil also in tonal conditions, giving some conclusions of the mechanisms of sound emissions by airfoils trailing edges.

3. ACKNOWLEDGEMENTS

The authors would like to thank engineer Odenir de Almeida for helping in some grid generation issues and for some discussions of the noise mechanisms.

4. REFERENCES

- Batten, P., Ribaldone, E., Casella, M., Chakravarthy, S., 2004, "Towards a Generalized Non-Linear Acoustics Solver", 10th AIAA/CEAS Aeroacoustics Conference, AIAA 2004-3001.
- Bobenrieth, R.F.M., Lauterjung, R.Q., Maldonado, A.L., Ribeiro, I.D., Godoy, K. and Garcia Neto, O., 2009, "Direct Computation of Noise Generated by Complex Geometries Using a High-Order Immersed Boundary Method", 15th AIAA/CEAS Aeroacoustics Conference, AIAA 2009-3181.
- Brooks, T.F., Pope, D.S., Marcolini, M.A., 1989, "Airfoil Self-Noise and Prediction", NASA Reference Publication 1218.
- Cho, Y., Boluriaan, S., Morris, P.J., 2006, "Immersed Boundary Method for Viscous Flow Around Moving Bodies", 44th AIAA Aerospace Sciences Meeting and Exhibit, AIAA 2006-1089.
- Desquesnes, G., Terracol, M., Sagaut, P., 2007, "Numerical investigation of the tone noise mechanism over laminar airfoils", *Journal of Fluid Mechanics*, vol.591, pp. 155-182, Cambridge-UK.
- Ghias, R., Mittal, R., Dong, H., 2007, "A sharp interface immersed boundary method for compressible viscous flows", *Journal of Computational Physics*, vol.227, pp.946-966.
- Kingan, M.J., Pearse, J.R., 2009, "Laminar boundary layer instability noise produced by an aerofoil", *Journal of Sound and Vibration*, doi:10.1016/j.jsv.2008.11.043.
- Liu, Q., Vasilyev, O.V., 2007, "A Brinkman penalization method for compressible flows in complex geometries", *Journal of Computational Physics*, vol.227, pp.946-966.
- McAlpine, A., Nash, E.C., Lowson, M.V., 1999, "On the generation of discrete frequency tones by the flow around an aerofoil", *Journal of Sound and Vibration*, vol. 222(5), pp 753-779.
- Nash, E.C., Lowson, M.V., McAlpine, A., 1999, "Boundary-layer instability noise on aerofoils", *Journal of Fluid Mechanics*, vol. 382, pp 27-61, Cambridge-UK.
- Peskin, C.S., 1972, "Flow patterns around heart valves: a numerical method", *Journal of Computational Physics*, vol.10, pp.252-271.
- Sandberg, R.D., Jones, L.E., Sandham, N.D., Joseph, P.F., 2008, "Direct numerical simulations of tonal noise generated by laminar flow past airfoils", *Journal of Sound and Vibration*, doi:10.1016/j.jsv.2008.09.003.
- Tam, C.K.W., 1974, "Discrete tones of isolated airfoils", *Journal of the Acoustical Society of America*.
- de Tullio, M.D., de Palma, P., Iaccarino, G., Pascazio, G., Napolitano, M., 2007, "An immersed boundary method for compressible flows using local grid refinement", *Journal of Computational Physics*, vol.225, pp.2098-2117.

5. RESPONSIBILITY NOTICE

The authors are the only responsible for the printed material included in this paper.